

DOE/ET-53088-129

IFSR #129

NONLINEAR INTERACTION OF TEARING MODES: A COMPARISON
BETWEEN THE TOKAMAK AND THE REVERSED
FIELD PINCH CONFIGURATIONS

J. A. Holmes, A. A. Carreras, T. C. Hender,
H. R. Hicks, and V. E. Lynch
Oak Ridge National Laboratory
Oak Ridge, Tennessee 37830

Z. G. An and P. H. Diamond
Institute for Fusion Studies,
University of Texas, Austin, Texas

March 1984

Nonlinear Interaction of Tearing Modes: A Comparison Between the Tokamak and the Reversed Field Pinch Configurations*

J. A. Holmes^a, B. A. Carreras, T. C. Hender, H. R. Hicks^a, and V. E. Lynch^a
Oak Ridge National Laboratory, Oak Ridge, Tennessee 37830

Z. G. An and P. H. Diamond
Institute for Fusion Studies, University of Texas, Austin, Texas 78712

ABSTRACT

The multiple helicity nonlinear interaction of resistive tearing modes is compared for the tokamak and reversed field pinch configurations using the magnetohydrodynamic equations. Unlike the case of the tokamak disruption, for which this interaction is destabilizing when islands overlap, the nonlinear coupling of the dominant helicities is shown to be a stabilizing influence in the reversed field pinch. The behavior of the coupled instabilities in the two configurations can be understood as a consequence of the stability properties of the nonlinearly driven modes. In the case of the tokamak disruption, quasi-linear effects linearly destabilize the dominant driven mode, which then feeds energy to the driving mode. For the reversed field pinch the driven modes remain stable, acting as a brake on the growth of the dominant instabilities. Furthermore, for the reversed field pinch configuration numerical results indicate that nonlinear coupling of different helicities results in noticeably more rapid saturation of the dominant instabilities than was observed in single helicity studies.

*Research sponsored by the Office of Fusion Energy, U.S. Department of Energy, under Contract No. W-7405-eng-26 with the Union Carbide Corporation.

I. INTRODUCTION

It has been suggested that in the reversed field pinch the sustainment of the reversed magnetic field configuration against transport processes may be due to the strong nonlinear interaction of resistive tearing modes.¹ On the other hand, the nonlinear interaction of resistive tearing modes in tokamaks has been shown to provide a mechanism capable of explaining and predicting major disruptions.^{2,3} In order to gain some understanding into how the nonlinear interaction of resistive tearing modes might give rise to such different behavior as dynamo action in the reversed field pinch and major disruptions in tokamaks, we compare the interaction of the dominant modes for the two configurations. We denote these modes by $(m;n)$ and the corresponding helicities by m/n , where m is the poloidal mode number and n the toroidal mode number. A simple tokamak disruption model has been found for which the dominant instabilities are the $(2;1)$ and $(3;2)$ tearing modes, while the dominant linearly unstable modes in reversed field pinch configurations are of type $(1;n)$ with $n \gg 1$.¹ In the tokamak disruption the main driven modes are the $(5;3)$ and $(1;1)$. The $(5;3)$ mode, with its singular surface lying between those of the $(3;2)$ and $(2;1)$ modes, plays the dominant role in the coupling.⁴ In the reversed field pinch the $(1;n)$ and $(1;n+1)$ modes are coupled by the $(2;2n+1)$ and $(0;1)$. The singular surface of the $(2;2n+1)$ mode lies between those of the $(1;n)$ and $(1;n+1)$ modes, while the singular surface for the $(0;1)$ is the field reversal surface. One could suspect that the $(2;2n+1)$ modes in the reversed field pinch will play a similar role to the $(5;3)$ mode in the tokamak disruption.

It is possible to describe several phases occurring in a tokamak disruption calculation. Starting with small perturbations of the (2;1) and (3;2) modes, these instabilities grow exponentially as independent linear eigenfunctions. As the perturbations become larger, the growth becomes algebraic due to quasi-linear effects,⁵ but the evolution still proceeds as for independent single helicities. The disruption is triggered when the nonlinear interaction between the (2;1) and (3;2) modes becomes strong, leading to the explosive growth of the (3;2) and other modes. This is followed by a turbulent stage involving the excitation and interaction of many modes.⁶ Because tokamak disruptions arise from a small number of spatially separated instabilities evolving in a low resistivity plasma, it is possible to observe the preturbulent phases clearly in numerical calculations truncated to include relatively few modes.

In the reversed field pinch configuration there are likely to be several unstable modes of type (1;n) with $n \gg 1$, all having singular surfaces in a region inside the field reversal surface. Because of the larger number of instabilities, the close spatial proximity of the unstable modes, and the large resistivity (in comparison with tokamaks), strong nonlinear interaction should dominate the evolution of reversed field pinch instabilities. In comparison with the phases of the tokamak disruption described above, nonlinear interaction becomes important early in the calculation, while the magnetic islands are still small. The numerical study of magnetohydrodynamic (MHD) turbulence and possible dynamo effects in reversed field pinches will

ultimately involve steady-state calculations with many interacting modes.

As an initial step, a comparison between the nonlinear interaction of tearing modes in tokamaks and in reversed field pinches is carried out here in three parts:

1. A brief review of the single helicity behavior of the dominant instabilities is given in Sec. III. For reversed field pinches, attention is given to the influence of the plasma beta and the location of singular surfaces.
2. This work concentrates on the effect of coupling two instabilities of different helicity. For the simple coupling scheme described above, a comparison is made between the tokamak and reversed field pinch configurations in Sec. IV.
3. Finally, we present in Sec. IV some initial considerations concerning the coupling of many modes. Although the excitation of many modes occurs only in the final stages of a tokamak disruption, any model for the dynamo in reversed field pinches that invokes resistive tearing modes must consider the presence of many such modes in a steady-state turbulent plasma.

In the following section (Sec. II) the assumptions and equations used in this work are discussed along with the equilibria used in these studies.

II. ASSUMPTIONS, EQUATIONS, AND EQUILIBRIUM

The behavior of resistive instabilities in reversed field pinches and in tokamaks is studied here using the resistive MHD equations in three spatial dimensions and time. For reversed field pinch calculations these equations are solved in the following form:

$$\frac{\partial \vec{B}}{\partial t} = \vec{v} \times (\vec{v} \times \vec{B} - \frac{1}{S_A} \eta \vec{J}), \quad (1)$$

$$\frac{\partial \vec{v}}{\partial t} = \vec{v} \times (\vec{v} \times \vec{v}) - \frac{1}{2} \vec{v} (v^2 + \beta_0 p) + \vec{J} \times \vec{B} + \frac{1}{R} \nabla_{\perp}^2 \vec{v}, \quad (2)$$

and an equation of state for the pressure which assumes either the form

$$\frac{\partial p}{\partial t} = -\vec{v} \cdot \vec{\nabla} p - \Gamma p \vec{v} \cdot \vec{v} + \frac{2}{\beta_0} (\Gamma - 1) \frac{\eta}{S_A} J^2 \quad (3a)$$

for a compressible plasma model or

$$\nabla^2 p = \frac{2}{\beta_0} \vec{\nabla} \cdot [\vec{v} \times (\vec{v} \times \vec{v}) - \frac{1}{2} \vec{v} v^2 + \vec{J} \times \vec{B} + \frac{1}{R} \nabla_{\perp}^2 \vec{v}], \quad (3b)$$

which constitutes an incompressible model ($\vec{\nabla} \cdot \vec{v} = 0$) similar to that used by Aydemir and Barnes.⁷

The plasma current satisfies the equation $\vec{J} = \vec{\nabla} \times \vec{B}$, and the magnetic field is divergence-free, $\vec{\nabla} \cdot \vec{B} = 0$. Equation (1) combines Faraday's law with the classical form of Ohm's law, whereas Eq. (2) is

the momentum equation. The specific form of the viscosity term appearing in Eq. (2) is strictly correct only when $\vec{\nabla} \cdot \vec{v} = 0$. Although the equation of continuity for the mass density is frequently included in the MHD equations, the mass density is assumed to be a constant ($\rho = \rho_0$) in this work. The effects of density perturbations upon the growth and evolution of resistive tearing modes are expected to be minor, so that the neglect of the equation of continuity is justified here. Equations (1)-(3) have been written in a dimensionless system of units with all lengths normalized to a (the plasma minor radius), the magnetic field \vec{B} to B_0 (the equilibrium toroidal vacuum field at the plasma major radius R_0), the velocity \vec{v} to the Alfvén velocity $v_A = (B_0^2/\mu\rho_0)^{1/2}$, the time to the Alfvén time $\tau_A = a/v_A$, the pressure p to p_0 (the equilibrium value at the magnetic axis), and the resistivity η to η_0 (the value at the magnetic axis). In terms of these quantities, $S_A = \tau_r/\tau_A$ is the ratio of the resistive skin time $\tau_r = a^2\mu/\eta_0$ to the Alfvén time; $\beta_0 = 2\mu p_0/B_0^2$ is the equilibrium beta at the magnetic axis; and $R = av_A/\nu$, where ν is the viscosity, in units of (a^2/τ_A) . The unit vector $\hat{\xi}$ denotes the toroidal (or axial in cylindrical geometry) direction, and the subscript \perp denotes the poloidal (perpendicular to $\hat{\xi}$) plane. Both the resistivity η and the viscosity coefficient R are taken to be constant in space and time. The ratio of specific heats is taken to be $\Gamma = 5/3$ in this work.

Because the evolution of resistive tearing modes is not extremely sensitive to toroidal curvature effects, cylindrical geometry is used here. Equations (1)-(3) are solved using an (r, θ, ξ) coordinate system. All physical quantities are required to be regular at the origin,

$r = 0$. Boundary conditions at the wall ($r = 1$) are taken to be $B_r = \tilde{J}_\theta = \tilde{J}_\zeta = v_r = \frac{\partial \tilde{p}}{\partial r} = \tilde{B}_\zeta(0;0) = 0$, where the superscript \sim denotes the value of the perturbation.

This system of equations is solved using the three-dimensional, nonlinear, initial value computer code CYL.⁸ The time-stepping scheme is partially implicit, using finite differences in the time and the radial coordinate r , and a spectral representation with periodic boundary conditions in θ and ζ . All time-dependent physical quantities are expressed in the form $f(r, \theta, \zeta, t) = \sum_{m,n} [f_{mn}^c(r, t) \cos(m\theta + n\zeta) + f_{mn}^s(r, t) \sin(m\theta + n\zeta)]$. Because of the up-down symmetry of the assumed equilibrium, it is possible to delete either the sine or cosine terms from each quantity and to refer unambiguously to the $(m;n)$ mode or component. In the numerical calculations a specific (finite) set of modes is included. This facilitates an understanding, through its inclusion or omission, of the role of each mode.

Whereas Eqs. (1)-(3) are equally valid for tokamaks and for reversed field pinches, the dominance of a nearly constant toroidal field in tokamaks may be used together with their large aspect ratio to derive a reduced set of equations.⁹ At low beta in cylindrical geometry, two scalar field equations in three spatial dimensions and time, one for the poloidal flux function ψ and the other for the velocity stream function ϕ , are obtained. These equations have been shown to provide results in excellent agreement with those of Eqs. (1)-(3) in the tokamak limit.⁸ These equations have been discussed extensively elsewhere,^{2,9,10} and, because they are significantly faster computationally than the full set of equations, they are used here,

rather than Eqs. (1)-(3), for tokamak cases using the RSF code described in Ref. 10.

We have studied Eqs. (1)-(3) using the following variations:

1. solving Eqs. (1)-(3a) as written (compressible fluid), including ohmic heating;
2. solving Eqs. (1)-(3a) (compressible fluid), without the ohmic heating term;
3. solving Eqs. (1)-(3b) as written (incompressible); and
4. deleting the resistive diffusion of the equilibrium, $\eta \vec{j}^{eq}$, from Eq. (1) for any of the above choices.

The compressible equations with ohmic heating lead to substantial increases in equilibrium pressure since no losses are included in the energy (pressure) equation. Although the rate of ohmic heating is inversely proportional to S_A , it is significant for experimental values ($S_A \gtrsim 10^4$). The deletion of the ohmic heating term in the compressible equations allows the initial plasma beta to be maintained throughout the calculation. For the incompressible equations, the equation of state can lead to a significant increase in pressure due to the fast resistive diffusion of the equilibrium. Sizeable pressure gradients are induced to maintain force balance with the $\vec{j} \times \vec{B}$ force resulting from this resistive diffusion. Turning off the resistive diffusion of the equilibrium eliminates this type of generation of $\vec{j} \times \vec{B}$ force and allows the study of the evolution of the resistive instabilities for a given equilibrium rather than for a sequence of equilibria related through resistive diffusion. Although results in this study are

presented using all four variations, it is arguable that without self-consistent resistivity profiles and energy loss mechanisms the neglect of equilibrium resistive diffusion and ohmic heating are the preferable options. In this case it is possible to focus on the stability and evolution for a particular equilibrium. However, the most important results presented here (namely, the effects of coupling instabilities of different helicity) are found to occur for all the above choices. From a practical standpoint it is easiest to make numerical computations using incompressibility because compressional Alfvén waves are then eliminated, allowing greater time step sizes and reduced computer time.

For the reversed field pinch calculations, the initial state has been taken to be a cylindrical, axisymmetric, ideal, zero flow equilibrium of Eqs. (1)-(3) plus a small perturbation. This equilibrium is a solution of the equation

$$\frac{\beta_0}{2} \frac{dp^{eq}}{dr} = -B_S^{eq} \frac{dB_S^{eq}}{dr} - \frac{B_\theta^{eq}}{r} \frac{d}{dr} (r B_\theta^{eq}) . \quad (4)$$

In order to solve Eq. 4 it is necessary to provide two additional relationships between the three unknowns p^{eq} , B_S^{eq} , and B_θ^{eq} . For the calculations here, this is done by specifying the pitch parameter

$$\mu(r) \equiv \frac{r B_S^{eq}}{B_\theta^{eq}} = \frac{q(r)}{\epsilon_L} , \quad (5)$$

where $\epsilon_L = 2\pi a/L$ with L being the length of the cylinder and a the minor radius, and the Suydam parameter¹¹

$$C(r) \equiv \frac{-\beta_0}{2} \frac{dp^{eq}}{dr} \frac{1}{r(B_S^{eq})^2} \left(\frac{\mu}{d\mu/dr} \right)^2. \quad (6)$$

The equilibrium is stable to localized pressure driven modes when $C(r) < 1/8$. For the calculations of this paper a zero beta equilibrium (due to Caramana et al.¹), which is stable to ideal modes but unstable to resistive tearing modes, has been chosen. This equilibrium was obtained by allowing the resistive evolution (according to a one-dimensional transport code¹²) of a tearing mode stable equilibrium due to Robinson.¹³ The parameters are $\mu(r) = 0.6125(1 - 1.8748r^2 + 0.8323r^4)$, $C(r) = 0$, and $\epsilon_L = 0.2$, which results in a safety factor profile $q(0) = 0.1225 \geq q(r) \geq q(1) = -0.005145$ with the field reversal surface at $r = 0.93$. The dominant $m = 1$ instabilities for this equilibrium have toroidal mode numbers in the range $10 \leq n \leq 15$ with $n = 11$ and 12 having the largest linear growth rates. Figure 1 shows the safety factor and current profiles for this equilibrium. Note the close spacing of the singular surfaces associated with the dominant instabilities.

For the reduced equations, as solved in RSF,¹⁰ the pressure does not appear in the dynamic equations and the toroidal magnetic field is assumed constant. Hence, an equilibrium solution is completely specified by giving the safety factor profile. For the calculations presented here we assume the functional form $q(r) = q_0$

$[1 + (r/r_0)^{2\lambda}]^{1/\lambda}$ with $q_0 = 1.344$, $r_0 = 0.56$, and $\lambda = 3.24$ (so that $q(0) = 1.344 \leq q(r) \leq q(1) = 4.32$). This equilibrium has been chosen because it is linearly unstable to both the (2;1) and (3;2) modes and because the evolution of these modes leads to strong nonlinear interaction and disruptive behavior for this equilibrium. The safety factor and toroidal current profiles for this equilibrium are shown in Fig. 1. Note the relatively large separation of the singular surfaces of the dominant instabilities when compared with those for the reversed field pinch.

III. SINGLE HELICITY CALCULATIONS

Before considering the coupling of instabilities having different helicities it is important to understand, as a reference point, the nonlinear evolution of a single helicity. For the instabilities involved in the tokamak disruption, the single helicity evolution has been studied and modeled in great detail,^{5,14-17} both numerically and analytically. For such instabilities the initial energy growth, which is exponential in time, slows to algebraic, due to quasi-linear effects, when the magnetic island width exceeds the tearing layer width. Eventually the instability saturates. For a given mode and equilibrium the linear growth rate, the algebraic growth of the magnetic island, and the saturation amplitude of the instability can all be estimated quasi-analytically.

The single helicity evolution of tearing modes in a reversed field pinch configuration has not been as thoroughly examined. Numerical calculations carried out by Caramana et al.¹ for the 1/10 helicity at $S_A = 10^3$ and the equilibrium described above show a double reconnection process in which a first reconnection of the magnetic island expels the original magnetic axis from the plasma, much the same as occurs for the $m = 1$ mode in sawtooth oscillations in tokamaks. However, this is followed by a second, slow reconnection in which the magnetic axis re-forms and moves back into the plasma at a rate proportional to $1/S_A$. These calculations were carried out using a fully compressible set of equations including the evolution of the mass density and ohmic heating.

In the present work, single helicity calculations are carried out at $S_A = 10^4$ for modes having poloidal mode number $m = 1$ and toroidal mode numbers $n = 10, 11$, and 12 . The singular surfaces for these helicities in the initial equilibrium are $r_{1/10} = 0.32$, $r_{1/11} = 0.38$, and $r_{1/12} = 0.43$, respectively (Fig. 1).

For the $m/n = 1/10$ helicity, complete reconnection of the magnetic island and expulsion of the magnetic axis followed by a slow, second reconnection and the re-emergence of the original magnetic axis (as described by Caramana et al.¹) is obtained using the compressible equations with ohmic heating and with the incompressible equations, including resistive diffusion of the equilibrium (see Figs. 2 and 3). When the ohmic heating term is turned off in the compressible equations and when the equilibrium resistive diffusion is turned off in the incompressible equations, the nonlinear growth of the instability saturates before expulsion of the magnetic axis (Figs. 2 and 4). For both double reconnection cases, beta increases substantially (Fig. 5) due to ohmic heating in the compressible case and to resistive diffusion and force balance in the incompressible case. Both of the saturating cases remain at low beta. As can be seen in Fig. 5, the Suydam criterion for stability to localized pressure-driven modes $[C(r) < 1/8]$ is violated at the $1/10$ singular surface quite early in both of the double reconnection cases. The evolution of the equilibrium to high beta is destabilizing in these cases. The dynamic growth rates for the magnetic and kinetic energies, defined by

$$\left. \begin{aligned} \gamma_M &= \frac{1}{2E_M} \frac{dE_M}{dt}, \\ \gamma_K &= \frac{1}{2E_K} \frac{dE_K}{dt}, \end{aligned} \right\} \quad (7)$$

where

$$\left. \begin{aligned} E_M &= \frac{1}{2} \int |\vec{B}|^2 d\tau, \\ E_K &= \frac{1}{2} \int |\vec{v}|^2 d\tau, \end{aligned} \right\} \quad (8)$$

are seen to follow closely the linear growth rates for the evolving equilibrium (Fig. 6), thus verifying the equilibrium evolution as the destabilizing factor.

For the $m/n = 1/11$ and $m/n = 1/12$ helicities, in which the singular magnetic surfaces lie farther from the magnetic axis, the magnetic islands saturate without expulsion of the magnetic axis (Fig. 7), regardless of the specific choice of dynamic equations. The maximum sizes of the islands obtained are, however, strongly dependent upon the choice of dynamics, with the larger islands resulting with increasing equilibrium beta. In Fig. 7 the magnetic axis is seen to move back toward the center late in the evolution, as in the second reconnection. This phenomenon is not observed when the resistive diffusion is turned off, so that the second reconnection is probably caused by the resistive diffusion of the equilibrium after the initial instability is saturated. For the $m/n = 1/12$ magnetic island, the results are similar to those for the $m/n = 1/11$, except that the maximum island sizes are smaller and the islands are farther from the center of the plasma.

IV. NONLINEAR COUPLING OF TWO UNSTABLE MODES

If the dynamo effect observed in reversed field pinch devices is caused by resistive tearing modes, it is almost certainly due to the nonlinear interaction of many such instabilities. Unlike tokamak profiles, for which at most a few tearing modes are unstable, there can be many unstable modes in reversed field pinches. Of these the dominant modes inside the field reversal surface are resonant with poloidal mode number $m = 1$ and high toroidal mode number $n \sim 10$. Because of the profiles in the reversed field pinch, the singular surfaces for these dominant modes are spaced fairly close together (Fig. 1) inside the field reversal surface. As a first step in understanding the interaction of these dominant instabilities, we focus here on the nonlinear interaction of two of these modes. It is instructive to compare and contrast this situation with the analogous one in tokamaks, which provides a well-understood theoretical model of the major disruption.^{2,4,6}

Using this model, we consider tokamak profiles in which both the $(m;n) = (2;1)$ and $(3;2)$ modes are linearly unstable. When these instabilities are small they grow independently, much as single helicity solutions. Consequently, the current profile is flattened around both the $m/n = 2/1$ and $3/2$ singular surfaces and steepened between these surfaces. During this time the $(5;3)$ mode is driven nonlinearly by the beating of the $(2;1)$ and $(3;2)$ modes. However, for certain profiles the steepening of the current gradient at the $5/3$ mode rational surface is sufficient to quasi-linearly destabilize the $(m;n) = (5;3)$ mode, which couples the $(2;1)$ and $(3;2)$ modes. After

this destabilization, the resonant coupling of the (2;1) mode with the (5;3) pumps energy into the (3;2) mode. The rapid growth which follows leads to the destabilization of other modes in a disruptive process.⁶

The destabilization of the (5;3) mode and the consequent explosive growth of the (3;2) have been studied analytically.^{4,6} In particular, it has been found that the nonlinear $\vec{J} \times \vec{B}$ force resulting from the coupling of the (5;3) and (2;1) modes after the destabilization of the (5;3) drives a rapid increase in the kinetic energy of the (3;2) mode. The analysis considers the growth of a test mode [the (3;2) mode] coupled by driven modes [dominated by the (5;3)] to a static background of modes [dominated by the (2;1)]. The influence of the background modes upon the growth of the test mode is found to depend upon the value of Δ' of the driven mode. For $\Delta' < 0$ the effect is stabilizing, and the nonlinear coupling damps the growth of the test mode. For $\Delta' > 0$, the nonlinear coupling drives the growth of the test mode, and the growth rate is estimated to be⁴

$$\gamma^2 \approx \frac{1}{\sqrt{\pi}} |\tilde{B}_r^{st}| \Delta' a^2 / (B_0 W \tau_{Hp}^2), \quad (9)$$

where \tilde{B}_r^{st} is the radial magnetic field of the static background, W is its radial extent, and Δ' is the value for the driven mode. Because this nonlinear effect is due to the $\vec{J} \times \vec{B}$ force, either when damped or driven, the effect of the nonlinear coupling upon the test mode appears first in the evolution of the kinetic energy. If Δ' of the driven mode is positive, the test mode will obtain a rapid growth on the MHD time scale. The test mode will have the structure of a localized vortex at

its singular surface, and one expects this nonlinear mechanism to trigger a rapid conversion of magnetic to kinetic energy.

Although Eq. (9) was derived under the assumptions of tokamak ordering, it is also valid at low beta in the interior of the reversed field pinch, away from the field reversal surface, where the toroidal field is significant. A discussion of nonlinear dynamics in reversed field pinches has been given in Ref. 18 with further details to follow in Ref. 19. Let us compare and contrast the coupling of the dominant modes in a tokamak disruption with that of the dominant modes for a reversed field pinch profile. In the tokamak disruption the test mode is taken to be the $(m;n) = (3;2)$ mode; the static background is dominated by the $(2;1)$ mode; and the $(5;3)$, with a singular surface between those of the $(3;2)$ and the $(2;1)$ modes, is the dominant driven mode. Numerical calculations at $S_{Hp} = 10^6$ show a destabilization of the $(3;2)$ mode with the kinetic energy growing most rapidly [Fig. 8(a)]. Prior to the destabilization of the $(3;2)$ mode, $\Delta'(5;3)$ becomes positive [Fig. 8(b)], and this quasi-linear destabilization changes the character of the mode [Fig. 8(c)]. No longer driven, the $(5;3)$ instability then pumps energy from the equilibrium into the vorticity of the $(3;2)$ mode, causing the destabilization observed in Fig. 8(a).

For the reversed field pinch equilibrium studied here, the largest linear growth rates are obtained for the $(m;n) = (1;11)$ and $(1;12)$ modes, respectively. The $(1;12)$ will be considered as the test mode, so the background is dominated by the $(1;11)$, and the dominant coupling mode is the $(m;n) = (2;23)$ with its singular surface between those of

the (1;11) and (1;12) modes. A nonlinear calculation at $S_A = 10^4$ shows that the (1;12) mode is stabilized noticeably more rapidly, in comparison to its single helicity behavior, by its coupling to the (1;11) mode [Fig. 9(a)]. The kinetic energy stabilization precedes that observed for the magnetic energy. The value of $\Delta'(2;23)$ remains less than zero throughout the calculation [Fig. 9(b)], and the character of this mode remains unaltered until the kinetic energy growth rate of the (1;12) mode becomes negative [Figs. 9(a) and (c)]. Hence, the (2;23) mode remains driven, extracting kinetic energy from the (1;12) mode and pumping it into the equilibrium. The nonlinear coupling of the (1;11) and (1;12) instabilities for this reversed field pinch profile is stabilizing. Although the results presented in Fig. 9 were produced using incompressible dynamics without resistive diffusion of the equilibrium (hence at low beta so that the model of Ref. 4 is applicable away from the field reversal surface), the same conclusions are obtained numerically when the other dynamic options are employed. The coupling is stabilizing and the (2;23) mode is not quasi-linearly destabilized.

It is appropriate to discuss the physics considerations which underlie the difference in nonlinear evolution of tearing modes in the tokamak and the reversed field pinch. In the tokamak, where $q \geq 1$, $q' > 0$, the resonant surfaces of the primary helicities, 3/2 and 2/1, are well separated. Hence, significant steepening of the current profile occurs as the 3/2 and 2/1 magnetic islands grow toward overlap. By way of contrast, in the reversed field pinch, where $q < 1$, $q' < 0$, the resonant surfaces of the primary helicities are quite closely

spaced. At initial overlap, the $1/n$ island has width $W_n \approx \frac{q}{n|q'|}$. Hence, little or no profile modification occurs before island overlap and the ensuing nonlinear coupling.

The difference between the results in the tokamak and reversed field pinch cases is consistent with the difference in $q(r)$ profiles and, ultimately, with the standing of each relative to the Taylor minimum energy state. In the tokamak configuration, which is relatively far from the minimum energy configuration, the widely separated unstable ($\Delta' > 0$) islands grow large enough prior to overlapping to distort the equilibrium current gradient, thus causing further instability. In the reversed field pinch configuration, which deviates (by resistive decay) only slightly from the minimum energy state, the closely spaced unstable islands do not grow large enough prior to overlapping to distort $\langle J \rangle'$. Hence, the driven $(2; 2n+1)$ mode remains stable ($\Delta' < 0$) and acts to stabilize the primary modes. Thus, tearing mode interaction does not lead to reversed field pinch disruption.

We now consider calculations involving a larger number of interacting modes. The nonlinear MHD calculations for the reversed field pinch configuration may be thought of as proceeding in three phases. The first phase involves the independent single helicity evolution of the dominant instabilities. Because of the large number of unstable modes and the close proximity of their respective singular surfaces, the duration of this phase is short. The second phase involves the nonlinear interaction of the dominant instabilities and is illustrated by a sequence of field line plots in Fig. 10. Several

magnetic islands, including the $m/n = 1/10 \rightarrow 1/14$, are visible in these plots. The interactions in this phase lead to spectrum broadening as the energy of the instability is spread among more and more modes. As discussed above, these interactions are stabilizing for the dominant modes. This is illustrated for the (1;11) mode in Fig. 11. The numerics of this run allow a large number (≈ 60) of modes to participate.

The final phase is turbulent, involving a broad spectrum of many modes. Using the incompressible equations, it is seen in Fig. 12 that the global energies do not change significantly as the number of modes included in the calculation is increased but that they are significantly different when a compressible model with no ohmic heating is employed. This illustrates the need for a proper energy evolution equation that incorporates in a self-consistent way the transport induced by tearing mode turbulence and edge effects. This subject will be considered in a separate publication.¹⁹

VI. CONCLUSIONS

The nonlinear evolution of resistive tearing modes for a reversed field pinch configuration has been examined numerically in cylindrical geometry using several variations of the full MHD equations. The details of the single helicity evolution depend upon the evolution of the equilibrium and upon the location of the singular surface. The double reconnection process described by Caramana et al.¹ is observed when the dynamics leads to sufficient beta and when the singular surface is close to the center of the plasma. Otherwise, the instability saturates prior to the first reconnection.

The nonlinear coupling of two unstable modes was considered in detail, and the behavior was contrasted with that observed in tokamak disruptions. Although the quantitative results depend upon the specific choice of dynamic equations, the coupling was seen to be stabilizing in all cases, unlike that in a tokamak disruption. This nonlinear stabilization can be understood in terms of an analytical model.^{4,6}

Finally, it was seen that this stabilization carries over to cases in which many modes are included. However, serious studies of turbulence in reversed field pinches will require a self-consistent transport model incorporating tearing mode turbulent transport and edge effects.

ACKNOWLEDGMENT

The authors wish to acknowledge useful discussions with M. N. Rosenbluth, R. A. Nebel, and D. D. Schnack.

This research was sponsored in part by the Office of Fusion Energy, U.S. Department of Energy, under Contract No. W-7405-eng-26 with the Union Carbide Corporation.

REFERENCES

- ^aUCC-ND Computer Sciences, Oak Ridge, Tennessee 37830.
- ¹E. J. Caramana, R. A. Nebel, and D. D. Schnack, Phys. Fluids 26, 1305 (1983).
- ²B. V. Waddell, B. A. Carreras, H. R. Hicks, J. A. Holmes, and D. K. Lee, Phys. Rev. Lett. 41, 1386 (1978); B. V. Waddell, B. A. Carreras, H. R. Hicks, and J. A. Holmes, Phys. Fluids 22, 896 (1979).
- ³H. R. Hicks, B. A. Carreras, J. A. Holmes, and V. E. Lynch, Nucl. Fusion 22, 117 (1982).
- ⁴B. A. Carreras, M. N. Rosenbluth, and H. R. Hicks, Phys. Rev. Lett. 46, 1131 (1981).
- ⁵P. H. Rutherford, Phys. Fluids 16, 1903 (1973).
- ⁶P. H. Diamond, R. D. Hazeltine, Z. G. An, B. A. Carreras, and H. R. Hicks, I.F.S. Report 116 (1983), accepted for publication in Physics of Fluids.
- ⁷A. Aydemir and D. C. Barnes, Proceedings of the U.S.-Japan Theory Workshop on 3-D MHD Studies for Toroidal Devices (ORNL CONF-8110101, Oak Ridge, 1981), p.187.
- ⁸J. A. Holmes, B. A. Carreras, T. C. Hender, H. R. Hicks, V. E. Lynch, and B. F. Masden, Phys. Fluids 26, 2569 (1983).
- ⁹H. R. Strauss, Phys. Fluids 19, 134 (1976).
- ¹⁰H. R. Hicks, B. A. Carreras, J. A. Holmes, D. K. Lee, and B. V. Waddell, J. of Comput. Phys. 44, 46 (1981).

- ¹¹B. R. Suydam, IAEA Geneva Conf. 31, 157 (1958).
- ¹²R. A. Nebel, R. L. Hagenson, R. W. Moses, and R. A. Krakowski, Los Alamos National Laboratory Report, LA-8185-MS, 1980.
- ¹³D. C. Robinson, Nucl. Fusion 18, 939 (1978).
- ¹⁴R. B. White, D. A. Monticello, M. N. Rosenbluth, and B. V. Waddell, in Plasma Physics and Controlled Nuclear Fusion Research (IAEA, Vienna, 1977), Vol. 1, p. 569.
- ¹⁵D. Biskamp and H. Welter, in Plasma Physics and Controlled Nuclear Fusion Research (IAEA, Vienna, 1977), Vol. 1, p. 579.
- ¹⁶R. B. White, D. A. Monticello, and M. N. Rosenbluth, Phys. Fluids 20, 800 (1977).
- ¹⁷B. A. Carreras, B. V. Waddell, and H. R. Hicks, Nucl. Fusion 19, 1423 (1979).
- ¹⁸Z. G. An, Bull. Am. Phys. Soc. 28, 1189 (1983).
- ¹⁹P. H. Diamond, private communication.

FIGURE CAPTIONS

FIG. 1. Equilibrium safety factor and current profiles for the reversed field pinch and tokamak cases considered in this paper. The singular surfaces of the dominant modes are indicated by arrows:

tokamak equilibrium — $r_{3/2} = 0.49$, $r_{5/3} = 0.56$, $r_{2/1} = 0.65$

reversed field pinch equilibrium — $r_{1/10} = 0.32$, $r_{1/11} = 0.38$,
 $r_{1/12} = 0.43$, $r_{1/13} = 0.47$, $r_{1/14} = 0.50$, $r_{1/15} = 0.52$,
 $r_{0/0} = 0.93$

FIG. 2. Magnetic island widths vs time for the single helicity cases discussed in the text. Expulsion and re-emergence of the magnetic axis are observed for the 1/10 mode in the incompressible and ohmically heated compressible calculations.

FIG. 3. Magnetic surfaces at several times for the 1/10 incompressible single helicity calculation. The expulsion and re-emergence of the magnetic axis can be seen.

FIG. 4. Magnetic surfaces at several times for the 1/10 compressible non-ohmically heated single helicity calculation. The island growth saturates without expulsion of the magnetic axis.

FIG. 5. $\langle \beta \rangle$ vs time for the 1/10 single helicity calculations considered here. For the cases characterized by expulsion and re-emergence of the magnetic axis, the beta increase is significant and the Suydam criterion is violated at the 1/10 singular surface during most of the calculation.

FIG. 6. (1;11) kinetic and magnetic energy growth rates vs time for the 1/11 single helicity incompressible calculation. The (1;11) linear growth rates for the evolved equilibrium show good agreement with dynamic growth rates.

FIG. 7. Magnetic surfaces at several times for the 1/11 incompressible single helicity calculation. The magnetic axis remains in the plasma throughout the calculation.

FIG. 8. Mode coupling in a tokamak disruption. (a) (3;2) kinetic and magnetic energy growth rates vs time for a tokamak disruption calculation and the single helicity magnetic energy growth rate. In the disruption, the (3;2) kinetic energy is destabilized first. (b) (5;3) magnetic energy growth rate compared with the average of the (2;1) and (3;2) kinetic and magnetic energy growth rates vs time. If the (5;3) mode were purely driven the curves would compare closely. Quasi-linear destabilization of the (5;3) mode occurs when $\Delta'(5;3)$ changes sign. (c) $\psi_{(5;3)}^{avg}$ vs time. The quasi-linear destabilization changes the character of the mode causing the turnover of the ψ_{avg} curve.

FIG. 9. Mode coupling for reversed field pinch profile. (a) (1;12) kinetic and magnetic energy growth rates vs time with coupled helicities, compared with the single helicity magnetic energy growth rate. With mode coupling, the (1;12) kinetic energy is stabilized first. (b) (2;23) magnetic energy growth rate compared with the average of the (1;11) and (1;12) kinetic and magnetic energy growth rates vs time. The close agreement between the curves as well as

$\Delta'(2;23) < 0$ indicates that the (2;23) mode remains driven.

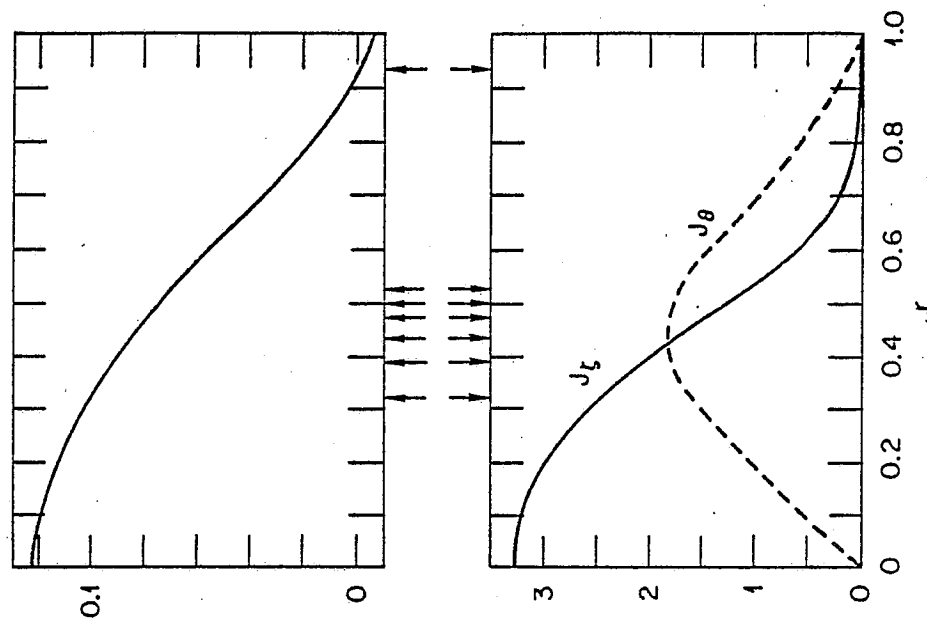
(c) $B_{(2;23)}^r$ vs time. The turnover occurs after the stabilization of the (1;12) mode.

FIG. 10. Magnetic field line plots showing the interaction of the dominant instabilities along the axial length of the reversed field pinch.

FIG. 11. (1;11) magnetic energy growth rate vs time in single helicity and coupled helicity reversed field pinch calculations. The nonlinear couplings are seen to be stabilizing.

FIG. 12. Total kinetic energies vs time for reversed field pinch calculations. The behavior is critically affected by the dynamic assumptions.

REVERSED FIELD PINCH



TOKAMAK

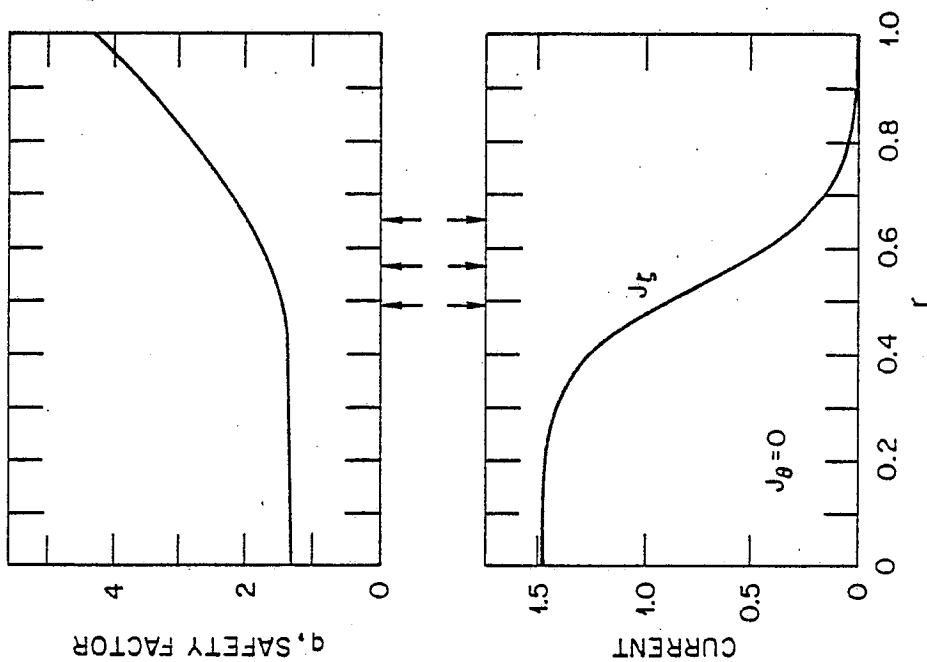


fig. 1

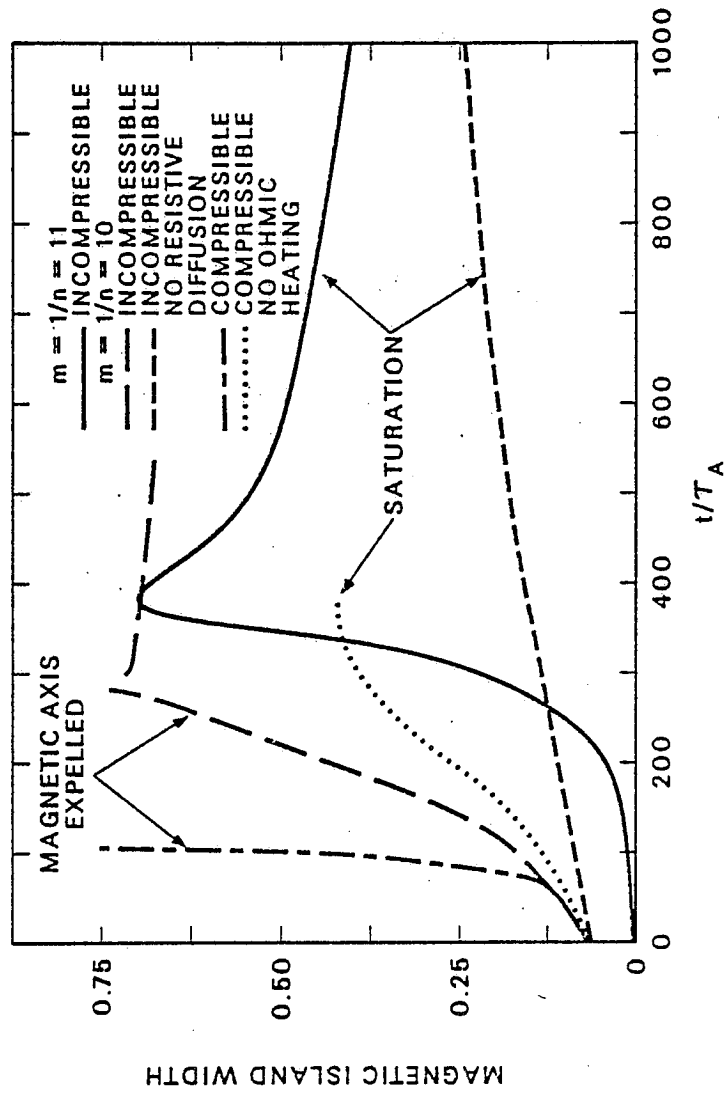


fig. 2

ORNL-DWG 83-4109 FED

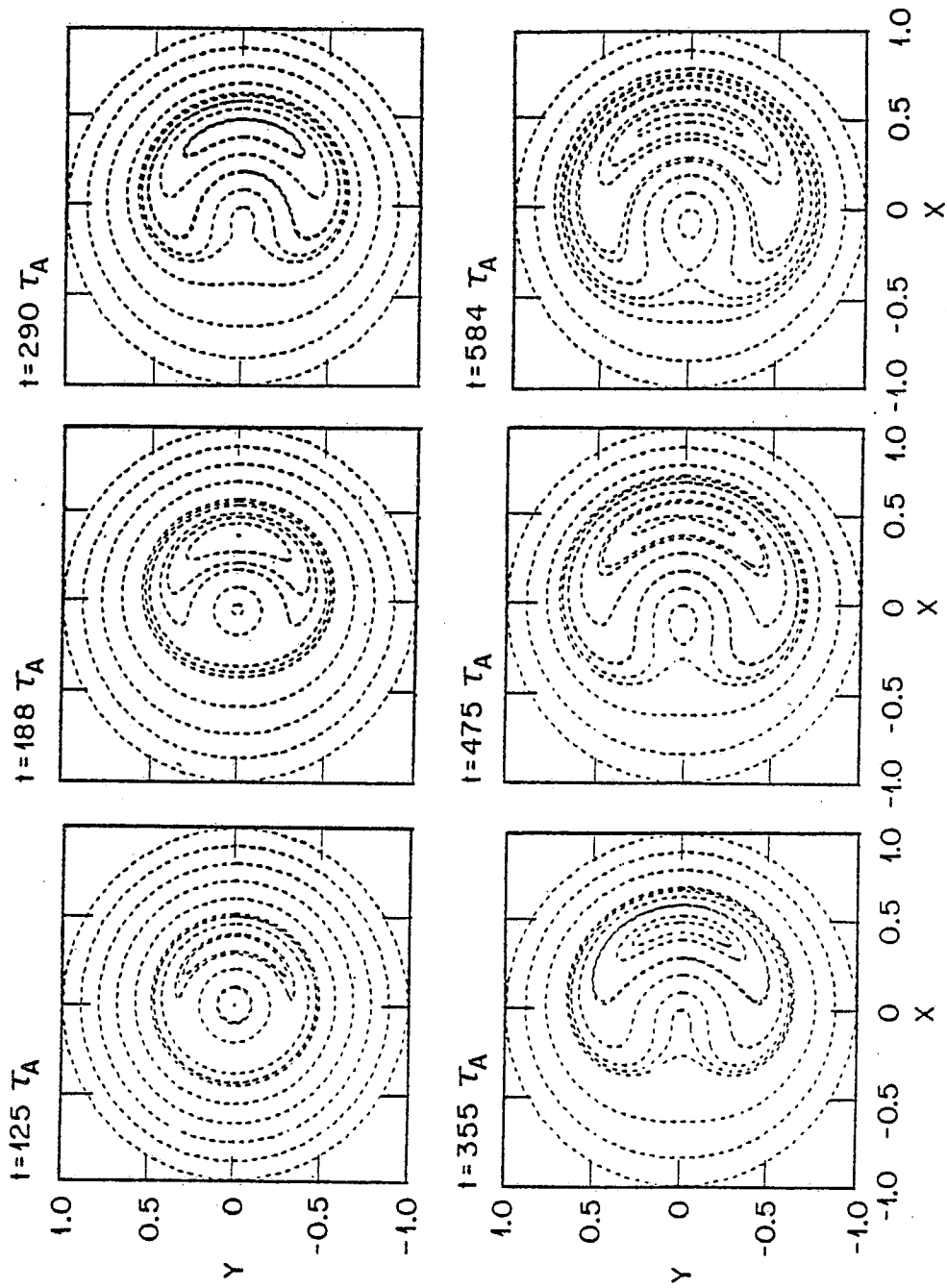


fig. 3

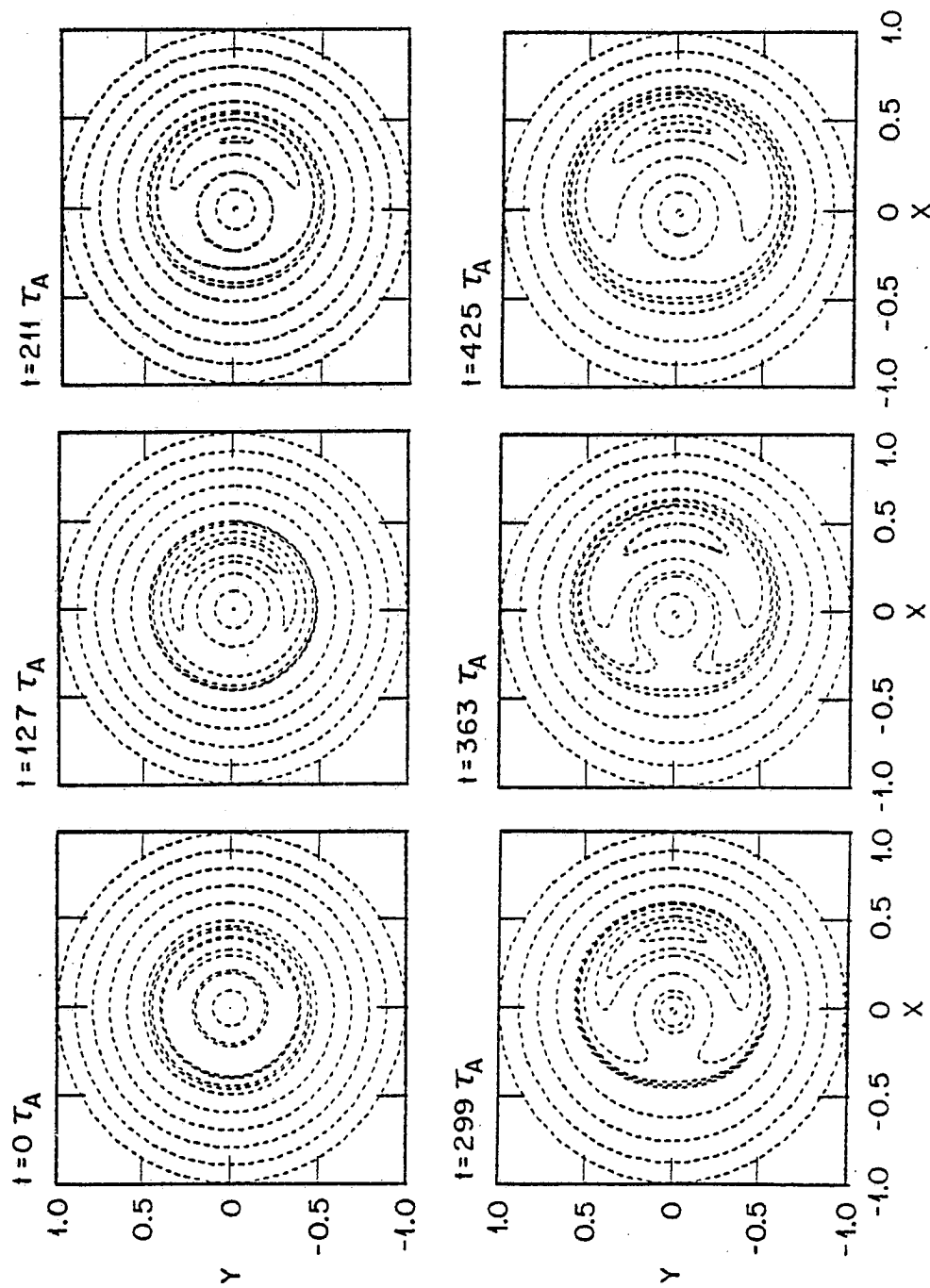


fig. 4

ORNL-DWG 83C-4101 FED

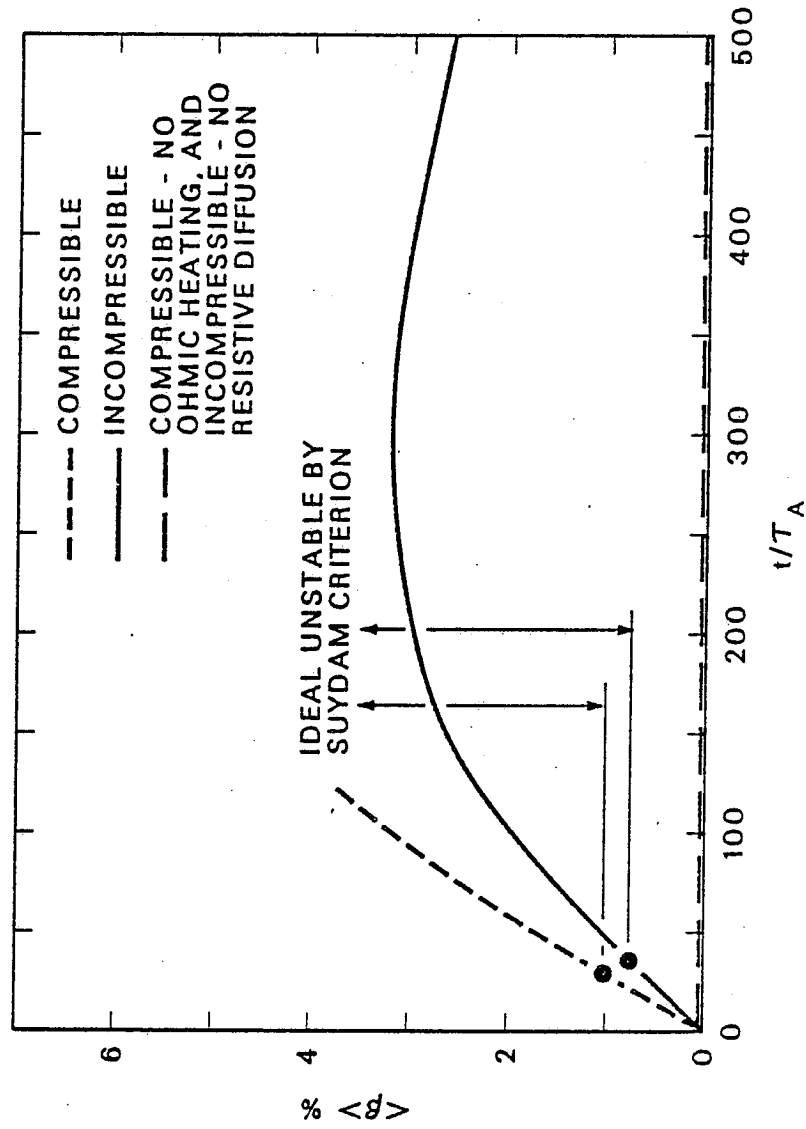


fig. 5

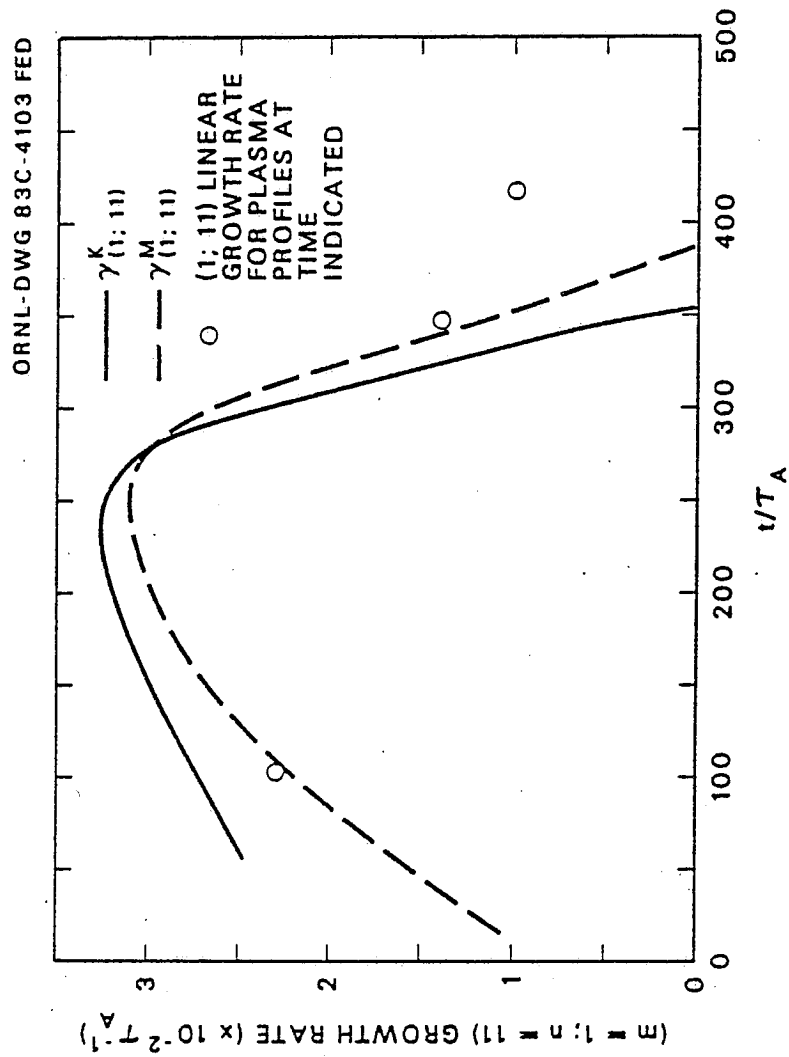
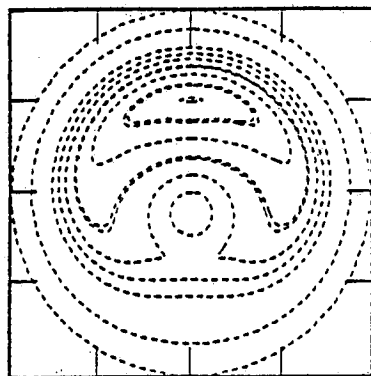


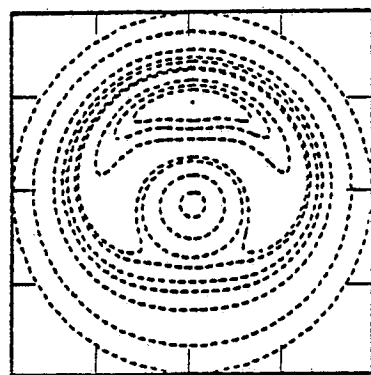
fig. 6

ORNL-DWG 83-4111 FED

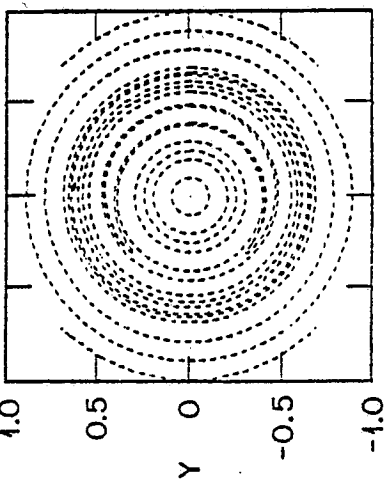
$t=374 \tau_A$



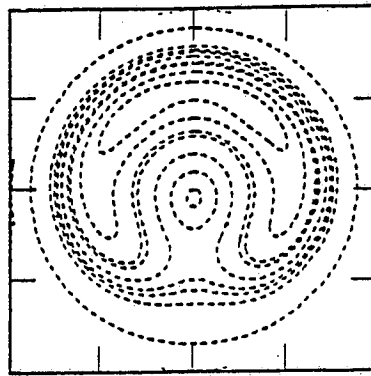
$t=348 \tau_A$



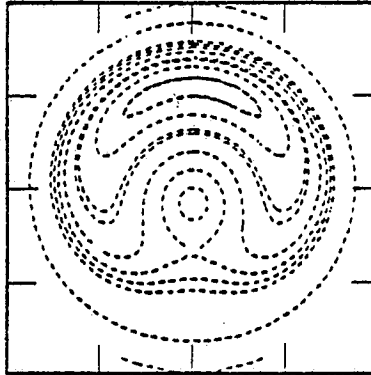
$t=253 \tau_A$



$t=440 \tau_A$



$t=411 \tau_A$



$t=391 \tau_A$

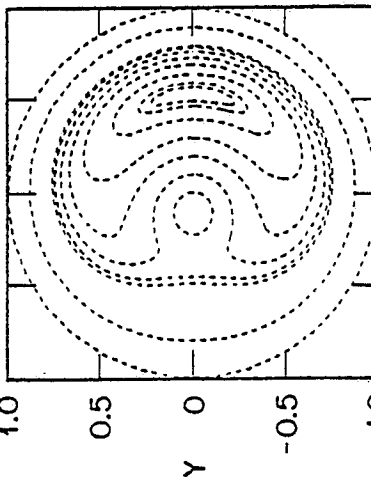


fig. 7

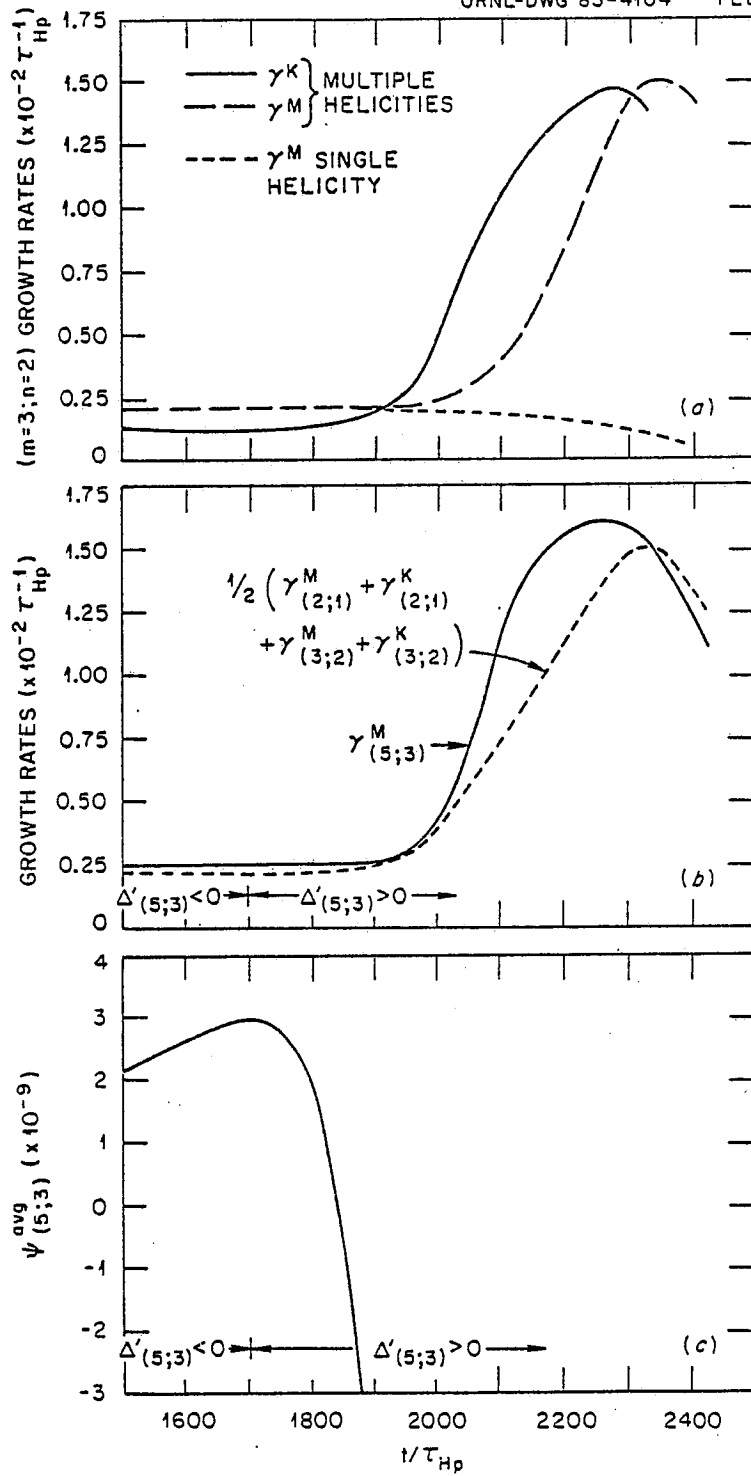


fig. 8

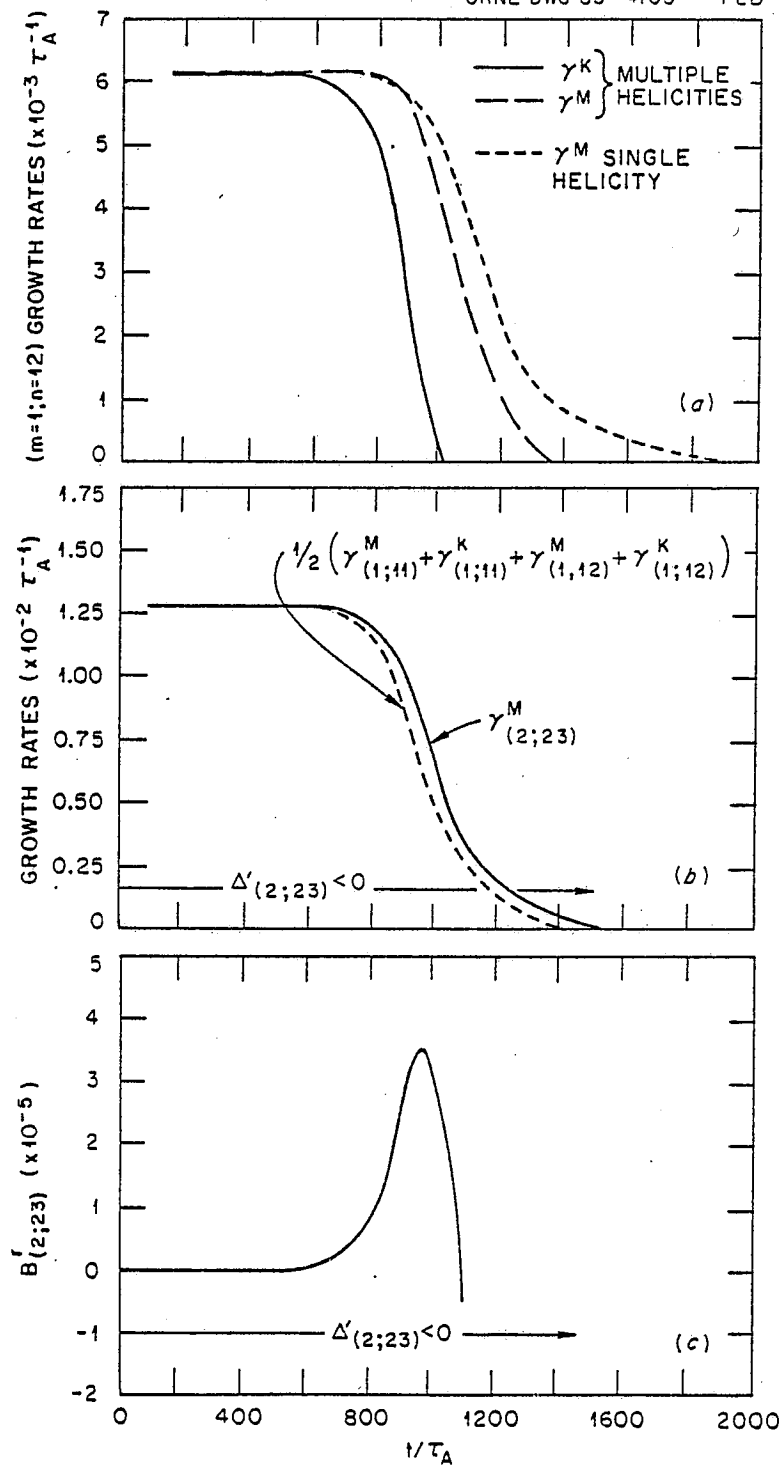


fig. 9

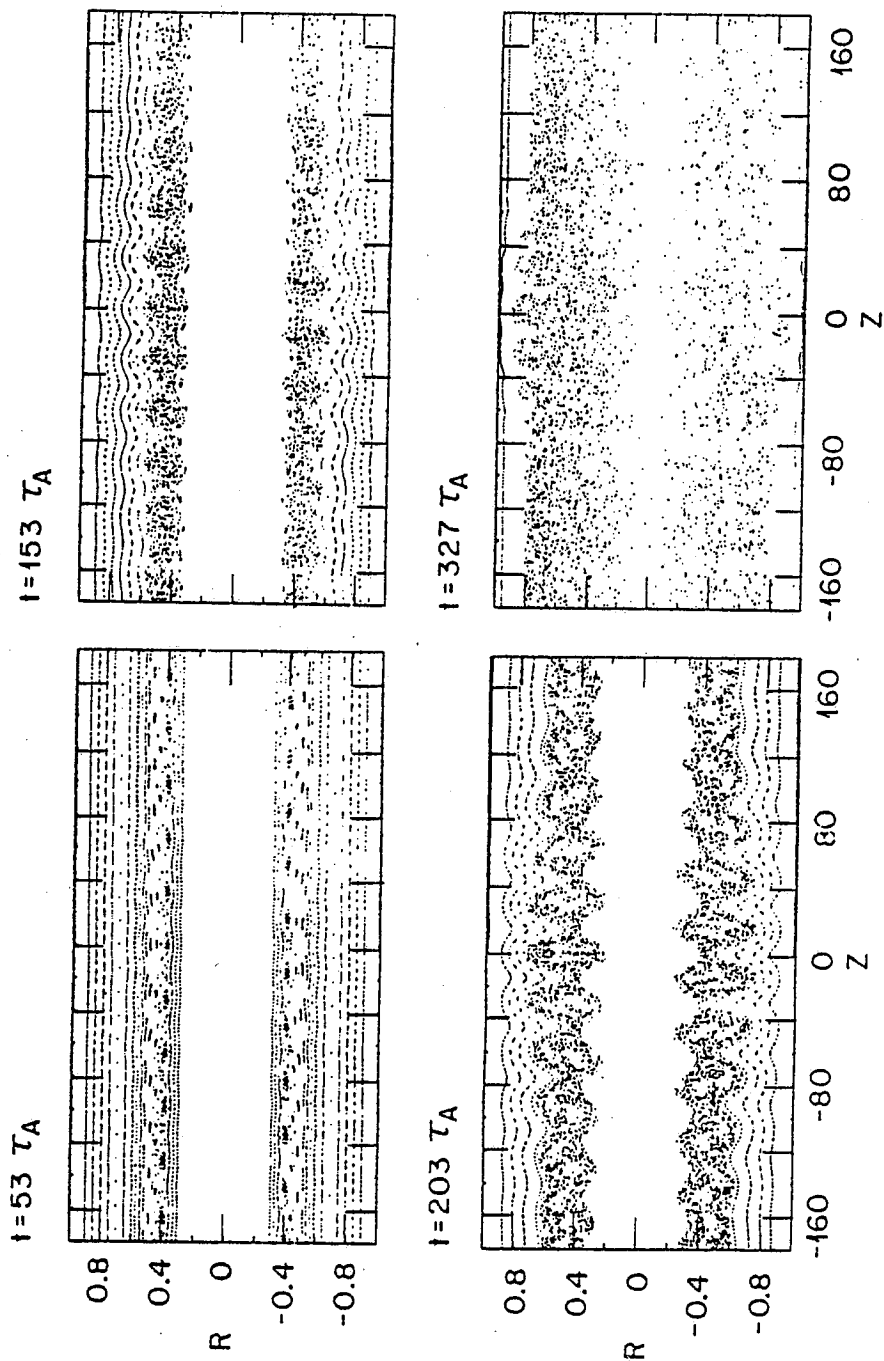


fig. 10

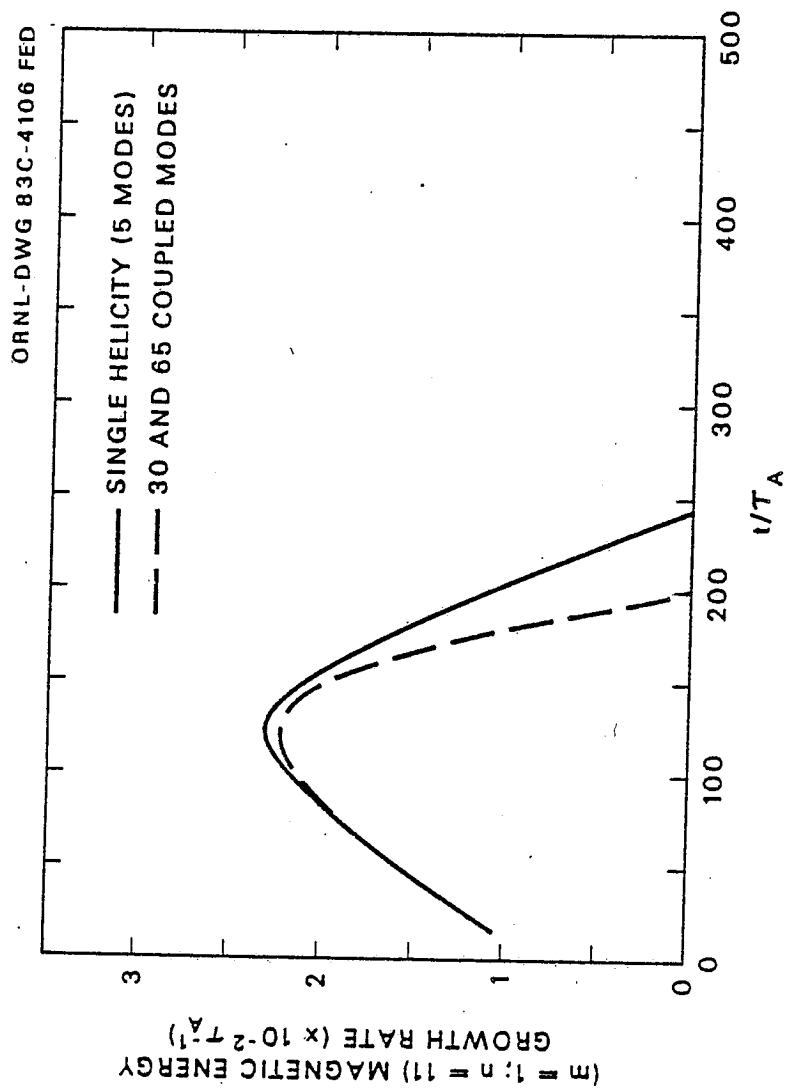


fig. 11

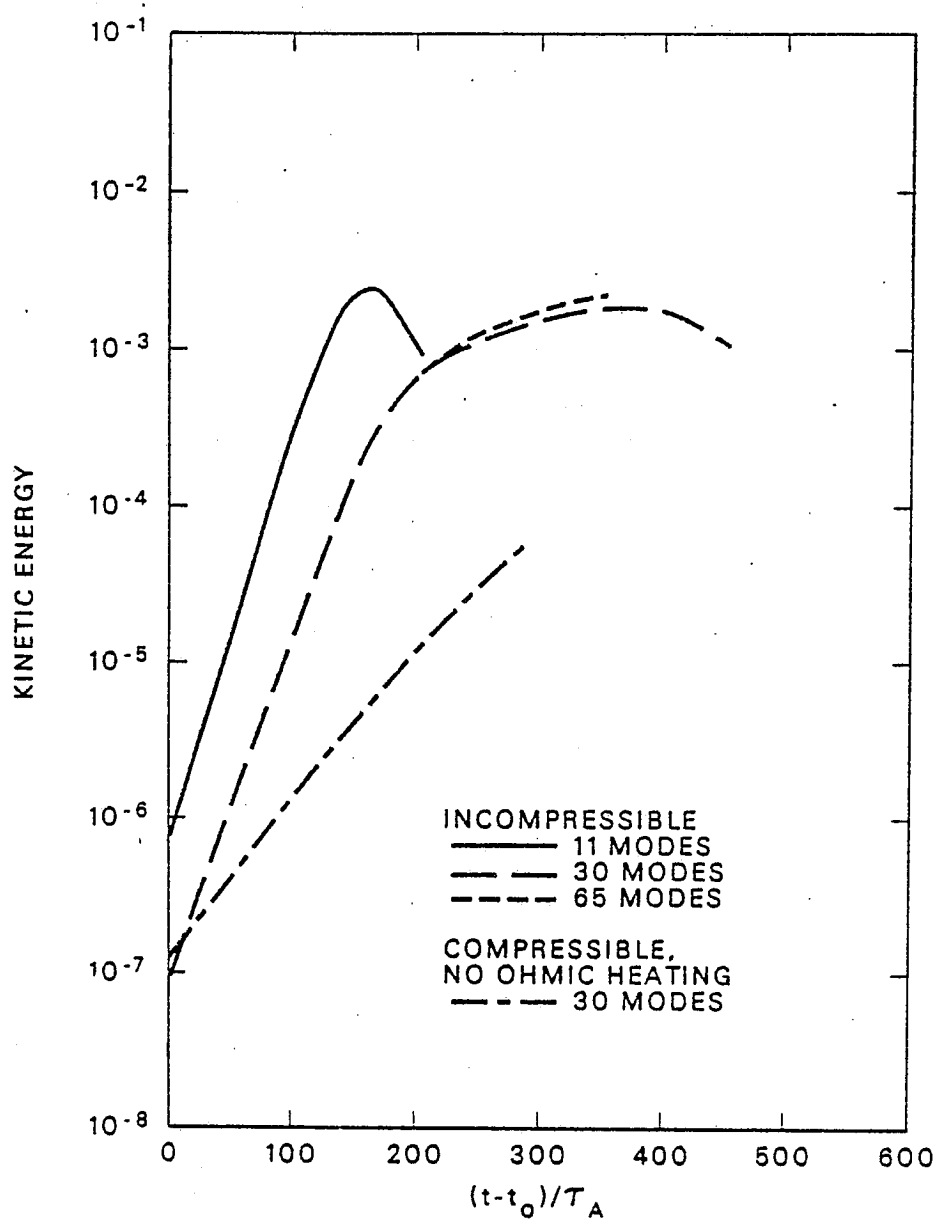


fig. 12